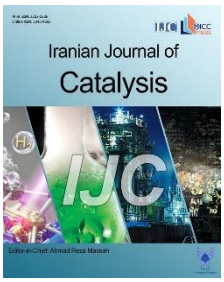

Volume 15, Issue 4, (2025) Article (1-18)

Iranian Journal of Catalysis (IJC)

https://doi.org/10.57647/j.ijc.2025.1504.41

Solar-Driven Degradation of Anionic Dyes Using Ultrasonically Synthesized Trimetallic Doped ZnO-Graphitic Carbon Nitride Nanocomposite Photocatalyst

Vaishali Sanjay Raut[1], Vishal Dnyaneshwar Pardeshi[2], Yogeshwar Rajaram Baste[1], Vijay Jotiba Naukudkar[2], Prashant Bhimrao Koli[3], Sachin Girdhar Shinde[4*]

[1]*Research Center in Chemistry, MVP Samaj's, KSKW College, CIDCO, Arts, Commerce and Science College Nashik, Maharashtra, India-422002, Affiliated to SPPU PUNE*
[2]*Research Centre in Chemistry, MVP Samaj's, KTHM Arts, Commerce and Science College, Nashik, Maharashtra, India-422002, Affiliated to SPPU PUNE*
[3]*Research Centre in Chemistry, MVP Samaj's, K.K.Wagh Arts, Science and Commerce College, Pimpalgaon (B), Taluka - Niphad, Dist-Nashik-422209, Affiliated to SPPU PUNE*
[4]*Research Center in Chemistry, K.V.N. Naik Arts, Commerce and Science College, Nashik, Maharashtra, India-422002, Affiliated to SPPU PUNE*

***Corresponding author:** sachings93@gmail.com

Original Research

Received:
21 February 2025

Revised:
19 May 2025

Accepted:
10 July 2025

Published online:
5 November 2025

Published in issue:
31 December 2025

Abstract

We report an ultrasound-assisted green synthesis of 2% Bi_2O_3, Co_3O_4, and Fe_2O_3 co-doped ZnO/g-C_3N_4 nanocomposites. Structural and physicochemical analyses (XRD, FTIR, SEM/EDS, UV–Vis DRS, BET) confirm uniform dopant incorporation, enhanced light harvesting, and increased surface area. Under natural sunlight, the composite achieved 98.1% degradation of Indigo Carmine and 94.8% degradation of Xylidine Ponceau within 90 min, as shown by UV–Vis and TOC measurements. Optimization of pH, catalyst loading, and dye concentration, coupled with radical scavenging assays, identified •OH radicals as the primary reactive species. The catalyst retained over 78% of its initial activity after four successive cycles, demonstrating outstanding stability and reusability. This work introduces a sustainable, low-energy route and a novel trimetallic doping strategy for efficient remediation of organic pollutants.

Keywords: Ultrasound-assisted synthesis; Doped ZnO-g-C_3N_4 nanocomposite; Solar-driven dye degradation; Indigo Carmine and Xylidine Ponceau; Photocatalysis

1. Introduction

Water pollution caused by industrial effluents containing organic pollutants is a growing environmental challenge, especially with the rapid expansion of industries in developed and developing countries [1]. Many industries, such as chemical, textile, paper, leather, and plastics, release large quantities of harmful organic chemicals like dyes, organic acids, pesticides, and detergents into nearby water bodies, which eventually end up in the oceans. These pollutants are often non-biodegradable and cause long-term damage to the environment, biosphere, and humans [2,3]. Dyes are especially more problematic organic contaminants compared to those mentioned before, because they can reduce light penetration from the surface into the water due to their low density compared to water, disrupting photosynthesis in aquatic plants, which is vital for oxygen production in water bodies. Moreover, due to their inertness and slow biodegradation, they incorporate a considerable amount of residue in water, causing carcinogenic and mutagenic
effects to smaller and eventually larger organisms [4]. These effects lead to oxygen depletion in water bodies,

decreasing the DO level, which results in an increase in BOD and COD in water [5]. Additionally, almost all dyes are carcinogenic, and their accumulation in the food chain can pose significant health risks .Water is a vital natural resource, yet its quality is increasingly threatened by organic pollutants, including synthetic dyes discharged from industrial processes [A, B]. Such contaminants pose serious environmental and health risks due to their toxicity and persistence [B].Photocatalytic dye degradation using advanced nanomaterials offers a promising route for water remediation, leveraging solar energy and eco-friendly mechanisms [4. 5]. Recent developments in semiconductor-based photocatalysts and optical strategies have significantly enhanced degradation efficiency and selectivity [6,7]. Sustainable management of water resources thus necessitates integrating green photocatalytic technologies to ensure long-term water safety and availability [8]. Advanced Oxidation Processes (AOPs) have emerged as highly effective strategies for the comprehensive elimination of organic pollutants from aqueous environments. Unlike conventional methods such as adsorption and flocculation, which often generate secondary waste, or membrane filtration, which requires sophisticated and costly infrastructure, AOPs offer a more sustainable and efficient alternative. Central to these processes is the use of photocatalysts that, upon light irradiation, absorb photons with energy equal to or greater than their band gap, thereby exciting electrons from the valence band to the conduction band and generating photoinduced electron–hole (e^-/h^+) pairs. These charge carriers interact with molecular oxygen (O_2) and water (H_2O) to form highly reactive oxygen species (ROS), primarily hydroxyl radicals (•OH) and superoxide anion radicals ($O_2^{\bullet-}$). The availability of more charge carriers enhances ROS generation, which in turn accelerates the degradation of organic dyes through mechanisms such as photo-Kolbe reactions. These reactive intermediates attack and oxidize complex organic molecules, leading to their mineralization into simpler inorganic end-products like carbon dioxide (CO_2), ammonia (NH_3), and water (H_2O). Such mineralization can achieve up to 98% reduction in organic carbon content, highlighting the efficacy of AOPs in advanced water purification [8,9].

Zinc oxide (ZnO) is a versatile and effective photocatalyst for dye degradation due to its structural flexibility, tunable bandgap, eco-friendliness, light absorption, and efficient charge separation factors crucial for high photocatalytic efficiency [10]. Zinc oxide (ZnO) is an excellent photocatalyst for dye degradation due to its wide band gap (~3.26–3.40 eV) and high exciton binding energy (~60 meV). These properties enable efficient absorption of UV light and stable generation of electron-hole pairs, which drive photocatalytic reactions. Upon excitation, ZnO produces reactive oxygen species (ROS) like hydroxyl radicals and superoxide ions that effectively degrade dye molecules. Variations in band gap energy depend on temperature, structure, and synthesis method, offering tunability for specific applications. Its high surface reactivity, chemical stability, abundance, low cost, and environmental friendliness make ZnO a promising material for photocatalytic wastewater treatment and other environmental remediation processes. Modifications such as doping with suitable metals extend its light absorption into the visible range, which is important for utilizing 42–50% of solar radiation. These modifications also improve charge transport and enhance the generation of reactive oxygen species [11, 12]. Furthermore, ZnO exhibits exceptional stability and reusability, maintaining its performance over multiple cycles. These characteristics make ZnO a promising candidate for environmental remediation through heterogeneous photocatalysis [13].

Recently, carbon-based materials like graphene oxide (GO), carbon nanotubes (CNT), and carbon fibers (CF) have found applications in various fields that require free electrons for different functions [14]. Among them, graphitic carbon nitride (g-C_3N_4) is a highly promising material for photocatalytic applications due to its unique properties, including a suitable bandgap (~2.7 eV) for visible light absorption, high thermal and chemical stability, and ease of synthesis from abundant precursors such as urea and melamine. Graphitic carbon nitride (g-C_3N_4), particularly in its tri-s-triazine-based form, exhibits a combination of mechanical robustness and semiconducting properties that make it highly suitable for photocatalytic and energy-related applications. Its two-dimensional conjugated polymeric structure contributes to a significant elastic modulus, reported to be approximately 210 ± 5 GPa for tri-s-triazine-based g-C_3N_4 (TgCN). The tensile strength also follows this trend, with values reaching 30 GPa for TgCN making it comparable to other strong 2D materials like graphene oxide [15]. However, pristine g-C_3N_4 demonstrates relatively low electrical conductivity, typically less than 1 S/cm, which limits its charge transport efficiency. This limitation can be overcome through structural modification or doping with conductive materials. For instance, the incorporation of semiconducting metalloids into g-C_3N_4 frameworks has been shown to enhance conductivity significantly, achieving values as high as 9.2 S/cm, which is nearly 24 times greater than that of unmodified g-C_3N_4. These enhancements not only improve the material's charge separation efficiency but also broaden its applicability in photocatalytic degradation with excellent reusability [16]. The 2D tri-s-triazine-based structure of g-C_3N_4 offers a matrix of empty orbitals, facilitating the efficient movement and storage of a large number of electrons generated on the surface of the excited semiconducting material. This structure effectively suppresses the recombination of photoinduced charge carriers, such as electrons (e^-) and holes (h^+), in the fabricated nanocomposite material [15, 16]. Moreover, its unique properties—such as enhancing the photocatalytic process, providing structural support, and increasing the overall surface area of nanocomposites—impart a synergistic effect that enables the generation of additional properties not found in individual semiconducting or carbon-based materials [16,17].

This study investigates the synthesis of trimetallic-doped ZnO semiconductors incorporating Bi_2O_3, Co_3O_4,

and Fe_2O_3 as dopants, selected for their distinct physicochemical properties. These dopants effectively modulate the bandgap of ZnO, thereby facilitating the transition of electrons to the conduction band while simultaneously suppressing electron–hole recombination [18]. Additionally, they enhance the structural integrity of the ZnO lattice and introduce oxygen vacancies or surface defects, which serve as active sites for dye adsorption and catalytic reactions—ultimately improving photocatalytic performance [19]. The incorporation of these dopants alters the electronic structure of ZnO, leading to enhanced light absorption and improved charge separation. This enhancement is attributed to their distinct bandgap energies (Bi_2O_3: ~2.8 eV; Fe_2O_3: ~2.2 eV; CoO: ~1.8 eV) [20,21]. Furthermore, their atomic radii (125–145 pm) are well-suited for substitution within the ZnO lattice. When coupled with g-C_3N_4, the doped ZnO materials demonstrate increased electron availability due to efficient excitation and inhibited charge recombination within the g-C_3N_4 matrix. This combination facilitates the generation of reactive oxygen species such as ·OH and O_2^-, which are instrumental in dye degradation. g-C_3N_4 thus functions both as an electron reservoir and as a favorable surface for dye adsorption, enhancing the photocatalytic degradation process. Moreover, dopant incorporation also modifies the surface area of the composite material, further promoting dye molecule adsorption and subsequent photodegradation into smaller, less harmful species [21,22].

Herein, Bi_2O_3, Co_3O_4, and Fe_2O_3 co-doped ZnO was synthesized by the hydrothermal method using urea as a fuel to obtain a high yield of trimetallic-doped ZnO semiconductor. The synthesized material was then coupled with g-C_3N_4, which was prepared by the pyrolysis of urea, followed by an ultrasound-assisted hydrothermal method. The resulting nanocomposite was tested for the degradation of Xylidine Ponceau (XP) and Indigo Carmine (IC) organic dyes under eco-friendly solar radiation. For comparison, pristine ZnO and g-C_3N_4 were also employed as photocatalysts.

2. Experimental

2.1. Materials

All chemicals were used as received without any further purification. Zinc nitrate hexahydrate ($Zn(NO_3)_2·6H_2O$, 97%), bismuth nitrate pentahydrate ($Bi(NO_3)_3·5H_2O$), iron nitrate nonahydrate ($Fe(NO_3)_3·9H_2O$), cobalt nitrate hexahydrate ($Co(NO_3)_2·6H_2O$), nitric acid (HNO_3), Indigo Carmine (IC), and Xylidine Ponceau (XP) were procured from Fisher Scientific, India. Urea ($CO(NH_2)_2$, 99%), polyethylene glycol 200 (PEG-200, 99.9%), isopropyl alcohol, EDTA, and benzoquinone were purchased from Merck, India.

2.2. Preparation of dye solution

Indigo Carmine (IC) and Xylidine Ponceau (XP), both anionic dyes (Figure 1), were selected as model organic pollutants for this study owing to their widespread applications in the textile, pharmaceutical, and food industries. Notably, anionic dyes are generally more resistant to degradation compared to cationic dyes, making them suitable for evaluating photocatalytic efficiency. Indigo Carmine (IC) and Xylidine Ponceau (XP) are synthetic azo dyes widely used in various industries, including textiles, cosmetics, and food products. However, their discharge into aquatic environments can pose significant ecological and health risks. IC, for instance, has been shown to cause adverse effects on aquatic organisms, including fish, algae, and invertebrates. Studies have demonstrated that IC can lead to the accumulation of toxic metabolites in aquatic organisms, disrupting metabolic pathways and causing cellular damage. Additionally, IC contributes to oxygen depletion in water bodies, negatively affecting aquatic life. Similarly, XP, due to its high molecular weight and complex aromatic structure, is persistent in the environment and poorly biodegradable, leading to long-term contamination of water resources. XP is also known to be toxic to aquatic life, inducing genotoxicity and mutagenicity in fish and other aquatic organisms. The intense coloration of these dyes further reduces light penetration in water, impairing photosynthesis in aquatic plants and disrupting the food chain. Therefore, the removal of these dyes from wastewater is critical for mitigating their hazardous effects on aquatic ecosystems and preserving environmental health. A stock solution of Indigo Carmine (100 $mg·L^{-1}$) was prepared using double-distilled water and subsequently diluted to the required concentrations for experimental analysis [18].

2.3. Synthesis of the Bi_2O_3, Co_3O_4, and Fe_2O_3 doped ZnO nanoparticles

Trimetallic-doped ZnO nanoparticles incorporating bismuth (Bi), iron (Fe), and cobalt (Co) were synthesized via the hydrothermal co-precipitation method. A calculated amount (10.31 g) of $Zn(NO_3)_2·6H_2O$ was added to 100 mL of 0.1 $mol·L^{-1}$ HNO_3 solution to ensure effective dissolution. Polyethylene glycol-200 (3.0 mL) was then added dropwise, and the mixture was stirred for 1 hour to obtain a clear solution. Subsequently, 1.2127 g of $Bi(NO_3)_3·5H_2O$, 1.0010 g $Fe(NO_3)_3·9H_2O$, and 0.7276 g $Co(NO_3)_2·6H_2O$ were added to achieve 2% doping of each of the dopants, followed by stirring for 2 hours. Urea (6 grams) was then introduced, and the mixture was stirred for an additional 3 hours. Nitric acid facilitated the dissolution of urea, resulting in an orange-colored clear solution. The homogeneous solution was dried in an open-air oven at 100 °C for 12 hours. The black residue obtained was then calcined at 450 °C for 3 hours, yielding a brownish-grey powder of Bi_2O_3, Co_3O_4, and Fe_2O_3 trimetallic-doped ZnO. The initial reaction was carried out in an aqueous medium, and a precipitate formed after 12 hours of heating, leading to the method being termed the hydrothermal co-precipitation method [19].

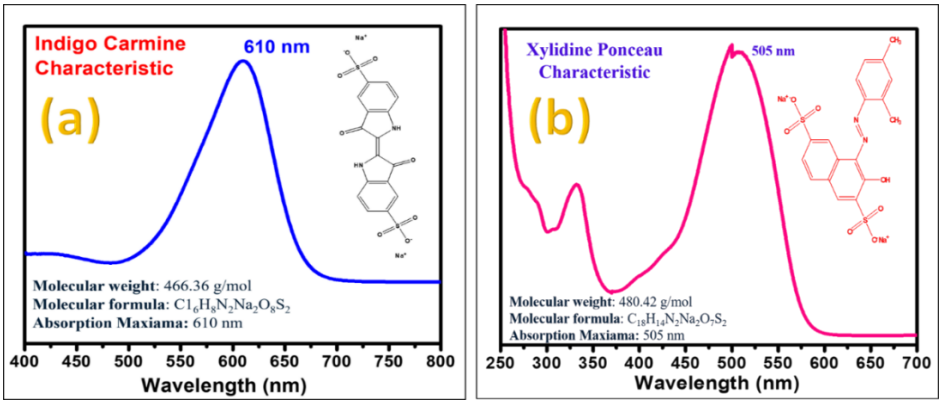

Figure 1. Molecular structures of anionic dyes: (a) Indigo Carmine and (b) Xylidine Ponceau

2.3. Synthesis of the Bi_2O_3, Co_3O_4, and Fe_2O_3 doped ZnO nanoparticles

Trimetallic-doped ZnO nanoparticles incorporating bismuth (Bi), iron (Fe), and cobalt (Co) were synthesized via the hydrothermal co-precipitation method. A calculated amount (10.31 g) of $Zn(NO_3)_2{\cdot}6H_2O$ was added to 100 mL of 0.1 $mol{\cdot}L^{-1}$ HNO_3 solution to ensure effective dissolution. Polyethylene glycol-200 (3.0 mL) was then added dropwise, and the mixture was stirred for 1 hour to obtain a clear solution. Subsequently, 1.2127 g of $Bi(NO_3)_3{\cdot}5H_2O$, 1.0010 g $Fe(NO_3)_3{\cdot}9H_2O$, and 0.7276 g $Co(NO_3)_2{\cdot}6H_2O$ were added to achieve 2% doping of each of the dopants, followed by stirring for 2 hours. Urea (6 grams) was then introduced, and the mixture was stirred for an additional 3 hours. Nitric acid facilitated the dissolution of urea, resulting in an orange-colored clear solution.

The homogeneous solution was dried in an open-air oven at 100 °C for 12 hours. The black residue obtained was then calcined at 450 °C for 3 hours, yielding a brownish-grey powder of Bi_2O_3, Co_3O_4, and Fe_2O_3 trimetallic-doped ZnO. The initial reaction was carried out in an aqueous medium, and a precipitate formed after 12 hours of heating, leading to the method being termed the hydrothermal co-precipitation method [19].

2.3.1. *Synthesis of Graphitic Carbon Nitride (g-C_3N_4)*

Graphitic carbon nitride (g-C_3N_4) was synthesized by heating 10 grams of urea at 550 °C in a muffle furnace for 3 hours, using a heating rate of 10 °C per minute. The final yield was 0.94 grams. This product was subsequently used to fabricate the nanocomposite [20].

2.3.2. *Synthesis of the Bi_2O_3, Co_3O_4, and Fe_2O_3 doped ZnO-g-C_3N_4 nanocomposite*

The ultrasound-assisted method was employed to synthesize trimetallic ZnO nanoparticles coupled with graphitic carbon nitride (g-C_3N_4).

Initially, 0.1 g of g-C_3N_4 was dispersed in 80 mL of 20% ethanol solution under stirring for 30 minutes, followed by ultrasonic irradiation (Vertilux 2Litre stainless steel ultrasonic bath; ultrasonic frequency: 40 kHz and ultrasonic power: 60 W) for 30 minutes to exfoliate bulk g-C_3N_4 into sheets. Subsequently, 1 g of trimetallic ZnO nanoparticles was added to the solution and stirred for 1 hour. The resulting suspension was then subjected to ultrasonic treatment for 3 hours (ultrasonic frequency: 40 kHz and ultrasonic power: 60 W), followed by continuous stirring for 12 hours. Finally, the product was filtered, washed with hot deionized water, and dried at 120 °C for 3 hours in an open-air oven to obtain grey-colored Bi_2O_3, Co_3O_4, and Fe_2O_3 co-doped ZnO–g-C_3N_4 nanocomposite [21].

2.3.3. *Characterization*

The morphology, grain size, crystallinity, and phase composition of the synthesized nanocomposites were characterized using transmission electron microscopy (TEM) and X-ray diffraction (XRD). XRD analysis was performed with a monochromatic Cu Kα radiation source (λ = 1.54060 Å) using a diffractometer operating at 45 kV and 40 mA, with a goniometer radius of 240 mm. Data were recorded at 25 °C between a 2θ range of 20°–90°, using a slit size of 0.8710°, step size of 0.017° 2θ, and a continuous scanning rate of 0.1° s^{-1}. TEM investigations were carried out using a Philips CM 200 microscope. Further morphological, compositional, and porosity analyses were conducted using scanning electron microscopy (SEM) and energy dispersive X-ray spectroscopy (EDAX) on a JSM 7600 F instrument. Functional groups were identified by Fourier-transform infrared spectroscopy (FT-IR) using a Bruker 3000 Hyperion Microscope coupled with a Vertex 800 FT-IR system. Optical properties were studied using UV-DRS, recorded on a JASCO V-750 UV-Visible Spectrophotometer equipped with an ISV-922 integrating sphere.

Surface area measurements were carried out using BET analysis on a Micromeritics Gemini 2375 and Gemini V system. TOC was analyzed by Mettler Toledo TOC analyzers. UV–Vis absorbance and photocatalytic dye degradation were evaluated with a Jasco V-730 double-beam spectrophotometer.

2.4. Photocatalytic Experiment:

The photodegradation efficiency of Bi_2O_3, Co_3O_4, and Fe_2O_3 co-doped ZnO-g-C_3N_4 nanocomposites was evaluated under eco-friendly solar radiation by

degrading two organic contaminants, namely Xylidine Ponceau (XP) and Indigo Carmine (IC), which are anionic organic dyes used in industries such as textiles, medicine, food, cosmetics, and pharmaceuticals. The synthesized nanocomposites were compared to commercial ZnO and g-C_3N_4 derived from the pyrolysis of urea. Figures 8(a) and (b) illustrate the degradation of XP and IC dyes in aqueous solutions under sunlight. A 100 mL dye solution, loaded with the catalyst, was directly exposed to sunlight with constant stirring between 12:00 PM and 3:00 PM on a summer afternoon. During this time, sunlight intensity was measured using a digital sun meter, with values ranging from 1100 to 730 W/m². Prior to photodegradation, an adsorption-desorption process was carried out for one hour in the dark. Aliquots were collected at regular time intervals and subjected to UV-Vis absorption measurements using a Jasco V-730 double beam spectrophotometer. The degradation percentages were calculated using Equation 3, and kinetic studies were conducted using Equation 4.

$$\% \, D = \frac{Co - Ct}{Co} \, X \, 100 \qquad (3)$$

Where, C_t serves as the dye's final concentration at a given time t, and C_0 is its initial dye concentration.

$$kt = -\ln \frac{C}{Co} \qquad (4)$$

Where, C represents the concentration (mgL^{-1}) in the solution phase, k, the rate constant, and C_o represents the concentration at time zero.

3. Results and Discussion

3.1. XRD analysis

X-ray diffraction (XRD) characterization plays a pivotal role in evaluating crystallinity, phase composition, structural purity or doping, and average crystallite size in synthesized nanomaterials.

The XRD patterns of commercial ZnO and Bi_2O_3, Co_3O_4, and Fe_2O_3 co-doped ZnO-g-C_3N_4 nanocomposites (Figure 2a and 2b) reveal sharp and well-defined diffraction peaks, indicative of high crystallinity. A prominent peak at 27.30°, corresponding to the (002) plane of graphitic carbon nitride (g-C_3N_4), confirms the incorporation of the carbonaceous matrix [25]. The observed reflections at 2θ values of 31.75°, 34.66°, 36.20°, 47.61°, 56.51°, 62.82°, 66.26°, 68.05°, and 69.05° correspond to the (100), (002), (101), (102), (110), (103), (200), (112), and (201) planes of the hexagonal wurtzite phase of ZnO, consistent with JCPDS data and literature reports [26].

Additional diffraction peaks at 23.50°, 33.48°, and 45.41°, corresponding to the (012), (311), and (220) planes, respectively, confirm the presence of Fe_2O_3, Co_3O_4, and Bi_2O_3 dopants within the ZnO-g-C_3N_4 matrix [27–29].

The successful incorporation of metal dopants and the formation of a homogeneous composite with g-C_3N_4 are thus validated by the combined XRD signatures. The crystallite size of the doped nanocomposites was estimated using the Debye–Scherrer equation (Eq. 1) [31], based on the most intense diffraction peaks. The average crystallite size of the Fe_2O_3, Co_3O_4, and Bi_2O_3 -doped ZnO-g-C_3N_4 was calculated to be approximately 36.19 nm, as presented in Table 1.

$$D = \frac{0.94 \, \lambda}{\beta \cos \theta} \qquad (1)$$

Where, λ is 1.5406 Å (the wavelength of Cu-Kα radiation), K is a constant (0.94), β is the full width at half maximum (FWHM), and θ is the diffraction angle [32,33].

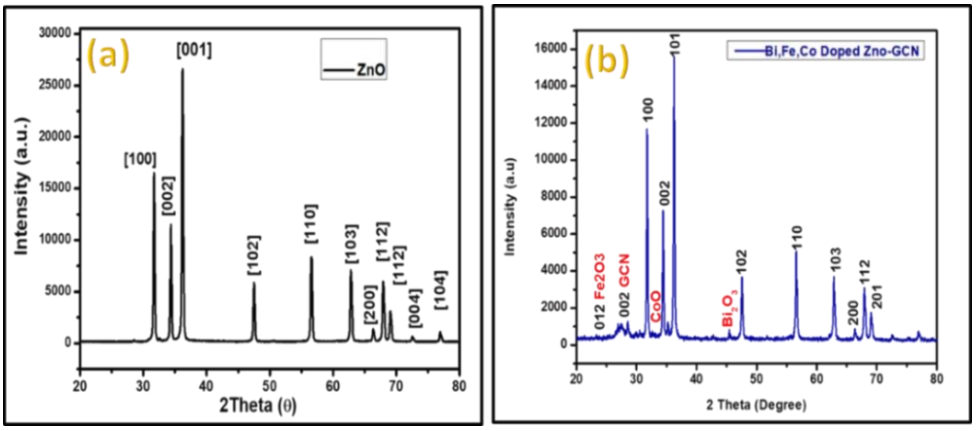

Figure 2. X-ray diffraction (XRD) patterns of (a) commercial ZnO and (b) Bi_2O_3, Co_3O_4, and Fe_2O_3 co-doped ZnO-g-C_3N_4 nanocomposite

Table 1. XRD-derived crystallographic parameters and crystallite size of Bi_2O_3, Co_3O_4, and Fe_2O_3 co-doped ZnO-g-C_3N_4 photocatalyst

2θ degree	Planes (hkl)	FWHM (β)	Size (nm)
36.25	101	0.194	31.22
31.75	100	0.173	37.86
34.45	002	0.19679	41.14
56.61	110	0.2993	34.49
47.56	102	0.2505	36.20
Average Crystallite Size = 36.19 nm			

3.2. TEM analysis

TEM measurements provide essential information regarding particle size, morphological features, crystal structure, and the effectiveness of the synthesis of Bi_2O_3, Co_3O_4, and Fe_2O_3 doped ZnO-g-C_3N_4 photocatalysts. The TEM images presented in Figure 3(a), corresponding to commercial ZnO nanoparticles, and Figure 3(b), depicting Bi_2O_3, Co_3O_4, and Fe_2O_3 doped ZnO-g-C3N4, show that the commercial ZnO nanoparticles form clusters of varying sizes. In contrast, the synthesized heterogeneous doped ZnO nanoparticles in Figure 3(b) are integrated with the g-C_3N_4 carbonaceous material using the ultrasound method [34]. The TEM image clearly demonstrates the successful deposition of nanoparticles onto the fabric-like surface of g-C_3N_4. This provides strong evidence for the effective synthesis of the nanocomposite using a simple and straightforward ultrasonic method.

3.3 SEM-EDS analysis

In this study, both commercial ZnO and synthesized trimetallic doped ZnO-g-C_3N_4were analyzed using a Scanning Electron Microscope (SEM), which offers high-resolution and magnification capabilities. The SEM image in Figure 4(a) shows clusters of nanoparticles in commercial ZnO. In contrast, the nanocomposite in Figure 4(b) reveals heterogeneous Bi_2O_3, Co_3O_4, and Fe_2O_3 doped ZnO- g-C_3N_4 nanoparticles attached to larger particles of graphitic carbon nitride (g-C_3N_4). This clustering increases the material's porosity, which is essential for photocatalytic applications due to its large surface area and excellent adsorption capacity [35]. Pollutants adhere to the surface through adsorption, a critical step for their subsequent degradation. The degradation process is most effective when adsorption is followed by degradation in the optimal sequence [36,37].

Energy-dispersive X-ray spectroscopy (EDS) was employed to determine the elemental composition of the Bi_2O_3, Co_3O_4, and Fe_2O_3 doped ZnO-g-C_3N_4 nanocomposite in comparison with commercial ZnO [38]. The EDS spectra shown in Figure 4(c) confirm the presence of all the doped elements, with no unexpected or unadded elements detected, unlike in Figure 4(a) for commercial ZnO [39].

The EDS results verify the successful incorporation of 1.83% bismuth, 1.96% iron, and 1.92% cobalt into the ZnO lattice, confirming approximately 2% doping of each element. Additionally, the data show that the material contains approximately 37.29% carbon and 20.35% nitrogen, which originate from the g-C_3N_4 carbon-based material.

This confirms the presence of graphitic carbon nitride in the Bi_2O_3, Co_3O_4, and Fe_2O_3 doped ZnO- g-C_3N_4 nanocomposite and its successful fabrication via the ultrasound method [40]. The detailed elemental composition of the synthesized material and commercial ZnO is provided in Table 2.

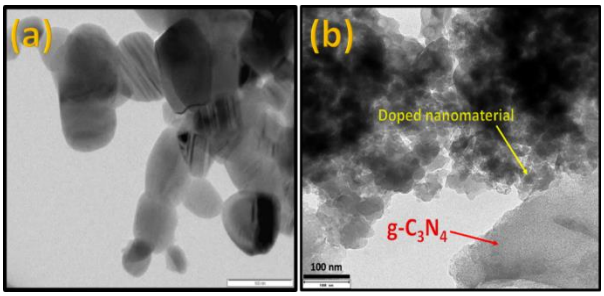

Figure 3. Transmission electron microscopy (TEM) micrographs of (a) commercial ZnO and (b) Bi_2O_3, Co_3O_4, and Fe_2O_3 co-doped ZnO-g-C_3N_4 nanocomposite

Table 2. Elemental composition (weight %) obtained from EDS analysis of commercial ZnO and Bi_2O_3, Co_3O_4, and Fe_2O_3 co-doped ZnO-g-C_3N_4 photocatalyst

Element	Atomic number	Weight (%)
Commercial ZnO		
O	9	29.33
Zn	30	70.67
		Total = 100
Bi_2O_3, Co_3O_4, and Fe_2O_3 doped ZnO-g-C_3N_4.		
C	6	37.29
N	7	20.35
O	9	12.71
Zn	30	23.94
Bi	83	1.83
Fe	26	1.96
Co	27	1.92
		Total = 100

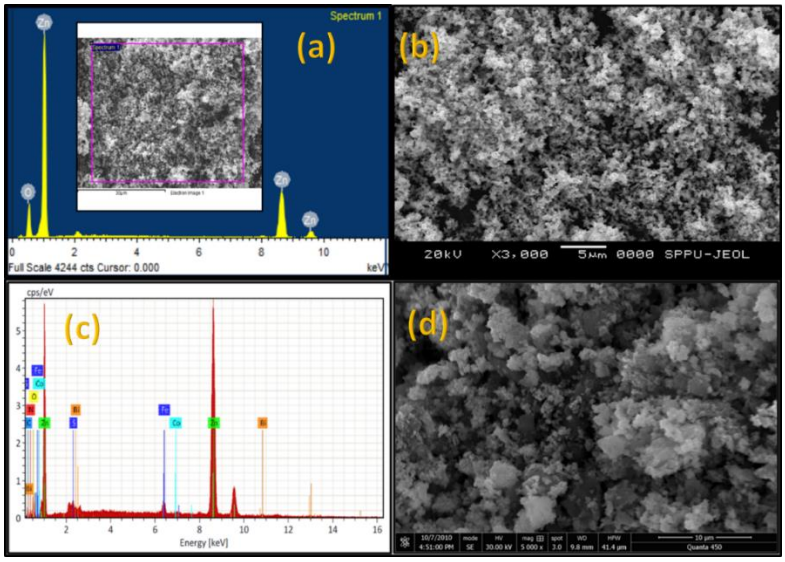

Figure 4. Scanning electron microscopy (SEM) and energy-dispersive X-ray spectroscopy (EDS) images of (a, b) commercial ZnO and (c, d) Bi_2O_3, Co_3O_4, and Fe_2O_3 co-doped ZnO-g-C_3N_4 nanocomposite

3.4. FT-IR analysis

Fourier-transform infrared (FT-IR) spectroscopy was employed to analyze the chemical bonding within the material. This technique is particularly important for carbon-based materials to confirm their structural integrity. The FT-IR spectra were recorded using a Vertex 800 FT-IR System from Bruker, Germany, over the frequency range of 400-4000 cm^{-1}. Figures 5 (a) and (b) show the FT-IR spectra of commercial ZnO and the synthesized Bi_2O_3, Co_3O_4, and Fe_2O_3 doped ZnO-g-C_3N_4 nanocomposite, respectively.

The FT-IR results provide strong evidence for the effective fabrication of doped ZnO nanoparticles on the 2D tri-s-triazine-based structure of graphitic carbon nitride (g- C_3N_4). In the synthesized nanocomposite, the absorption band between 3384 and 3015 cm^{-1}, featuring two distinct peaks, corresponds to the stretching frequencies of O-H bonds (from adsorbed water molecules) and N-H bonds (from g- C_3N_4) [40]. The peaks observed at 1636, 1403, and 1242 cm^{-1} are characteristic of graphitic carbon nitride's tri-s-triazine rings, corresponding to the stretching vibrations of C=C, C=O, C=N, and C-N bonds, respectively [41,42].

The presence of metallic dopants in the synthesized material is confirmed by FT-IR spectra, which display characteristic M–O stretching vibrations: Zn–O at 809 cm^{-1}, Fe–O at 881 cm^{-1}, Co–O at 738 cm^{-1}, and Bi–O at 558 cm^{-1}. These distinct absorption bands verify the successful incorporation of all metal dopants. Notably, this analysis also underscores the absence of g-C_3N_4 in bare ZnO. In the FT-IR spectrum of commercial ZnO (Figure 5(a)), peaks associated with O–H stretching and H–O–H bending vibrations are present; however, no additional peaks corresponding to the triazine ring structure of graphitic carbon nitride are observed. The FT-IR spectra thus confirm the successful incorporation of nanoparticles with g- C_3N_4, leading to the effective formation of the Bi_2O_3, Co_3O_4, and Fe_2O_3 doped ZnO-g-C_3N_4 nanocomposite.

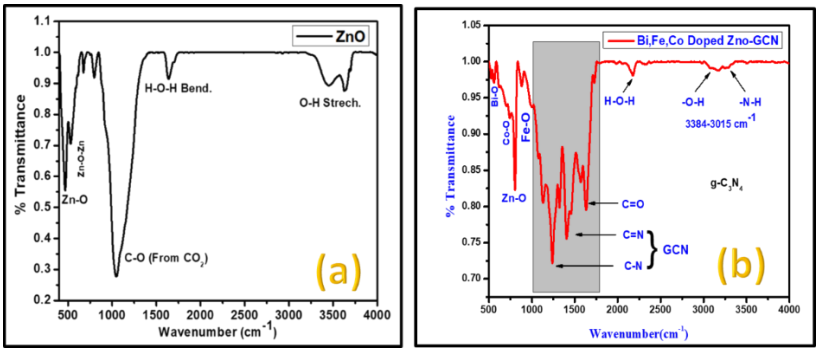

Figure 5. Fourier-transform infrared (FT-IR) spectra of (a) commercial ZnO and (b) Bi_2O_3, Co_3O_4, and Fe_2O_3 co-doped ZnO-g-C_3N_4, highlighting metal–oxygen bonding and doping-related features

3.5. Optical properties

UV Diffuse Reflectance Spectroscopy (UV-DRS) was employed to investigate the fabrication and activity of the material in the visible range of radiation, which is crucial for harnessing solar energy, as the visible spectrum constitutes nearly 43% of total solar radiation. Figures 6 (a) and (c) display the UV-DRS absorbance spectra, while Figures 6 (b) and (d) present the Tauc plots for commercial ZnO and the Bi_2O_3, Co_3O_4, and Fe_2O_3 doped ZnO-g-C_3N_4 nanocomposite, respectively, calculated from the DRS data.

The absorption peak observed around 290 nm for commercial ZnO indicates its limited activity in the visible region. In contrast, the Bi_2O_3, Co_3O_4, and Fe_2O_3 doped ZnO-g-C_3N_4 nanocomposite exhibits a noticeable absorption peak around 363 nm, and the broader UV-DRS spectrum indicates significantly improved activity under visible light radiation.This red shift in the synthesized material is attributed to the doping of visible light-active, lower band-gap materials such as Bi_2O_3, Co_3O_4, and Fe_2O_3 into the ZnO lattice, as well as the incorporation of the active, visible-light-harnessing g-C_3N_4 2D material [43].

Equation 2 was applied to the UV-DRS analysis results to determine the band gap energy of both commercial ZnO and the Bi_2O_3, Co_3O_4, and Fe_2O_3 doped ZnO-g-C_3N_4 from the corresponding Tauc plots.

$$(\alpha h\nu) = A(h\nu - Eg) \quad (2)$$

In the equation, (αhν) represents the absorption coefficient, which indicates the rate at which a material absorbs photons. A is a constant, and hν refers to the photon energy [44].

The synthesized photocatalyst exhibits a band gap (Eg) of 2.92 eV, which is significantly lower than that of pure ZnO (3.17 eV). This reduction in the band gap is a notable finding, providing substantial evidence that the doping of Bi_2O_3, Co_3O_4, and Fe_2O_3 and the incorporation of g-C_3N_4 have effectively reduced the band gap. Such a reduction is expected to enhance the photocatalytic efficiency of the material by extending its activity into the visible light spectrum.

This observation further supports the critical role of doping and composite formation with carbonaceous materials in improving photocatalytic performance.

3.6. BET surface area study

The Brunauer–Emmett–Teller (BET) surface area analysis was conducted to assess the surface properties of both materials, as the catalyst surface plays a significant role in photocatalytic contaminant degradation. Effective adsorption is crucial for the degradation of organic contaminants. Figure 7(a) illustrates the adsorption isotherm for pure ZnO, where the x-axis represents the relative pressure (P/P_0), and the y-axis indicates the volume of gas adsorbed (cm^3/g). The graph demonstrates a gradual increase in adsorption volume at lower relative pressures, followed by a sharp rise as the relative pressure increases [45]. This behavior is characteristic of a type IV isotherm, commonly observed in mesoporous materials. The sharp increase at higher pressures indicates multilayer adsorption and capillary condensation occurring within the mesoporous ZnO structure [46]. While ZnO exhibits reasonable adsorption capacity, its surface area and porosity are limited, as reflected by the modest adsorption volume. The surface area of commercial ZnO is 38 m^2/g, which is consistent with previously reported data [47].

Figure 7(b) shows the adsorption isotherm for the Bi_2O_3, Co_3O_4, and Fe_2O_3 doped ZnO-g-C_3N_4 composite, which demonstrates a significantly higher adsorption volume compared to pure ZnO, particularly at higher relative pressures. The surface area of this composite is

98 m²/g, considerably greater than that of commercial ZnO [48]. The sharp rise in adsorption suggests enhanced porosity and surface area, resulting from the incorporation of g-C_3N_4 carbonaceous 2D material and the effective doping into the ZnO structure. The presence of g-C_3N_4 likely introduces additional mesopores and increases the number of surface-active sites, improving the material's adsorption properties [49]. This enhanced adsorption capacity makes the trimetallic ZnO-g-C_3N_4 composite more suitable for applications requiring a high surface area, such as photocatalysis and pollutant removal. A comparison between the two materials clearly highlights the superior performance of the nanocomposite, demonstrating the effectiveness of structural modifications in enhancing the functional properties of ZnO-based materials [50].

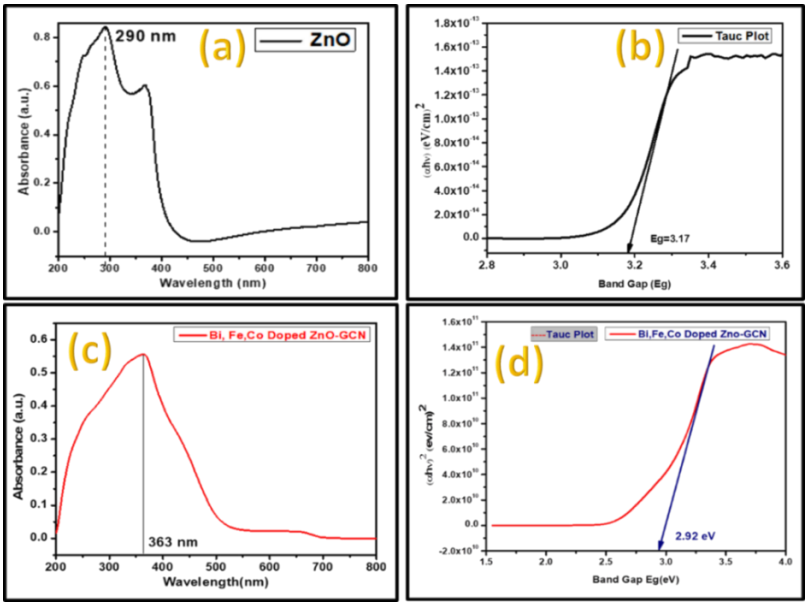

Figure 6. UV–visible diffuse reflectance spectroscopy (UV-DRS) and corresponding Tauc plots of (a, b) commercial ZnO and (c, d) Bi_2O_3, Co_3O_4, and Fe_2O_3 co-doped ZnO-g-C_3N_4 nanocomposit

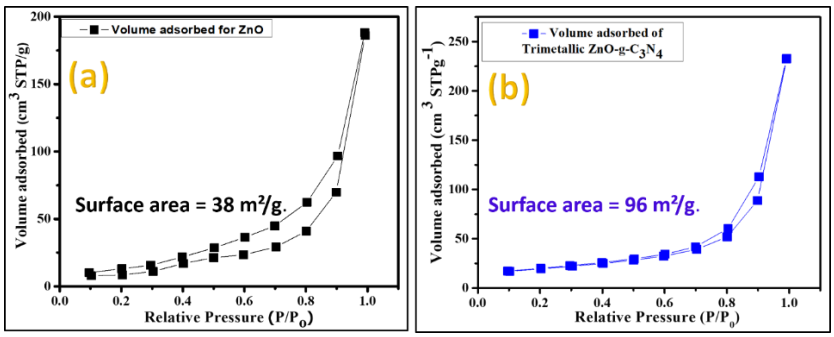

Figure 7. Brunauer–Emmett–Teller (BET) surface area analysis of (a) commercial ZnO and (b) Bi_2O_3, Co_3O_4, and Fe_2O_3 co-doped ZnO-g-C_3N_4 nanocomposite

3.6. Photocatalytic activity of the nanocomposite

The synthesized trimetallic Bi_2O_3, Co_3O_4, and Fe_2O_3 co-doped ZnO–g-C_3N_4 nanocomposite photocatalyst exhibited significantly enhanced photocatalytic activity for the degradation of the anionic dyes Indigo Carmine (IC) and Xylidine Ponceau (XP) under natural solar irradiation, in comparison to both commercial ZnO and thermally synthesized graphitic carbon nitride (g-C_3N_4), as detailed in Section 2.3.1. As shown in Figures 8 (a) and (b), degradation efficiencies reached 98.14% for IC and 94.82% for XP within 90 minutes of solar exposure, highlighting the superior light-harvesting capability and improved charge carrier dynamics of the doped system.

The photodegradation kinetics were found to follow the Langmuir–Hinshelwood (L–H) model, indicating a surface-mediated catalytic process where dye adsorption and subsequent photoreaction govern the overall rate. The pseudo-first-order rate constants (k) were calculated using the linearized form of the kinetic equation $\ln(C_0/C_t) = kt$, as illustrated in Figures 9 (a) and (b) and summarized in Table 3. For the Bi_2O_3, Co_3O_4, and Fe_2O_3 co-doped ZnO–g-C_3N_4 composite, the k values were 0.02488 min^{-1} for IC and 0.01903 min^{-1} for XP, reflecting rapid degradation kinetics. In contrast, commercial ZnO exhibited lower rate constants of 0.01015 min^{-1} (56.02% degradation of IC) and 0.00554 min^{-1} (41.24% for XP), while pristine g-C_3N_4 showed intermediate values of 0.01791 min^{-1} (63.11% for IC) and 0.00990 min^{-1} (49.23% for XP).

The enhanced photocatalytic activity of the trimetallic-doped nanocomposite can be ascribed to synergistic

effects such as enhanced visible-light absorption due to electronic band structure modification, increased density of surface oxygen vacancies, and effective separation of photogenerated electron–hole (e^-/h^+) pairs facilitated by heterojunction formation. Moreover, the incorporation of transition metal dopants introduces defect states within the bandgap, acting as trapping sites to delay recombination and thereby enhancing the photocatalytic redox potential.

The high linear regression coefficients ($R^2 > 0.98$ for both dyes) support the applicability of the pseudo-first-order kinetic model under the assumptions of the L–H mechanism, indicating that the photodegradation process is predominantly surface-reaction limited. These results collectively confirm the kinetic superiority and photocatalytic robustness of the Bi_2O_3, Co_3O_4, and Fe_2O_3 doped ZnO–g-C_3N_4 nanocomposite for environmental remediation under solar light irradiation [51]. The enhanced photocatalytic performance of Bi_2O_3, Co_3O_4, and Fe_2O_3 co-doped ZnO-g-C_3N_4 is attributed to the high surface area of the composite and the incorporation of Bi_2O_3, Co_3O_4, and Fe_2O_3, which enhance the generation of photoinduced charge carriers (e^-/h^+ pairs) while suppressing their recombination due to the trapping of electrons in g-C_3N_4 and the conduction bands of the dopant materials [52].The significant improvement in photocatalytic efficiency is also linked to the optimized band gap energy (Eg = 2.92 eV) of the nanocomposite, which enables effective utilization of solar energy and promotes the generation of reactive oxygen species, such as HO• and $O_2^{\bullet-}$. Overall, the synthesized material proved to be much more effective than commercial ZnO and g-C_3N_4 for organic contaminant degradation. Figure 10 (a) and (b) shows the continuous color fading of both dye contaminants within 90 minutes of solar radiation, with an inset picture displaying aliquots of the degraded dye sample, which demonstrates excellent degradation of both anionic dyes [53].

3.7. Effect of pH

The degradation efficiency of IC and XP dyes using Bi_2O_3, Co_3O_4, and Fe_2O_3 co-doped ZnO-g-C_3N_4 is significantly influenced by the pH of the reaction mixture. The physical and chemical interactions between the catalyst and the contaminant molecules are greatly affected by the pH in heterogeneous photocatalysis. pH also influences the production, stability, and activity of reactive oxygen species (ROS), such as HO• and $O_2^{\bullet-}$ radicals [54]. The pH of 100 mL, 10 mg L^{-1} dye solutions for both IC and XP anionic dyes was varied from 2 to 10 by adding dilute HCl/NaOH, with a catalyst dose of 0.4 g, under sunlight (Figure 11).

The highest degradation efficiency for both IC and XP was observed at pH 8, which is attributed to the enhanced generation of ROS, including HO• and $O_2^{\bullet-}$ [55]. At pH values higher than 8, the degradation capacity decreased for both dyes, indicating that ROS were effectively scavenged by carbonates and bicarbonates generated in the highly alkaline medium [56]. Additionally, the catalytic surface may undergo excessive hydroxylation, leading to increased repulsion of the negatively charged contaminants [57]. At pH values below 6, the degradation efficiency drastically decreased, likely due to the wear and dissolution of the catalyst surface and limited ROS generation. Furthermore, previous studies have reported that lower pH is unfavorable for the stability of g-C_3N_4 carbonaceous material. In summary, a slightly alkaline pH (around pH 8) favors the degradation of anionic dye contaminants under sunlight.

Zeta potential analysis was performed to assess the surface charge characteristics of the synthesized nanocomposite, which is a critical parameter influencing colloidal stability. Surface charge, whether positive or negative, contributes significantly to nanoparticle dispersion through electrostatic repulsion, thereby minimizing aggregation. The measurement was carried out using distilled water as the dispersion medium.As illustrated in Figure 12, the carbon-based nanocomposite exhibited a zeta potential of –3.84 mV, indicating a negatively charged surface. This negative surface charge is primarily attributed to the presence of hydroxyl (–OH) functional groups on the catalyst surface, a commonly reported feature in carbonaceous nanocomposite systems [58].

Table 3. First-order rate constants (k) for the photocatalytic degradation of Indigo Carmine and Xylidine Ponceau using Bi_2O_3, Co_3O_4, and Fe_2O_3 co-doped ZnO-g-C_3N_4 (reaction conditions: catalysts, 0.4 g/100 ml; dye concentration, 10 mg/L; pH, 8.0)

Photocatalyst	Indigo Carmine (IC)		Xylidine Ponceau (XP)	
	k (min^{-1})	R^2	*k* (min^{-1})	R^2
ZnO	0.01015	0.9961	0.00554	0.9960
g-C_3N_4	0.01791	0.9972	0.00990	0.9936
Bi_2O_3, Co_3O_4, and Fe_2O_3 doped ZnO-g-C_3N_4	0.02488	0.9981	0.01903	0.9977

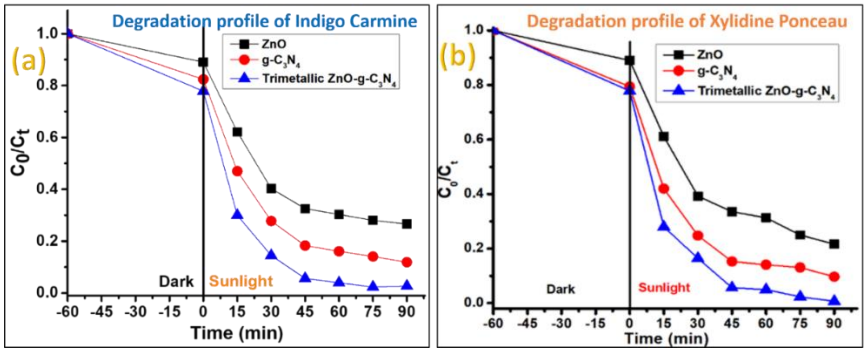

Figure 8. Photocatalytic degradation performance of Bi_2O_3, Co_3O_4, and Fe_2O_3 co-doped ZnO-g-C_3N_4 nanocomposite under solar irradiation for (a) Indigo Carmine and (b) Xylidine Ponceau (reaction conditions: catalysts, 0.4 g/100 ml; dye concentration, 10 mg/L; pH, 8

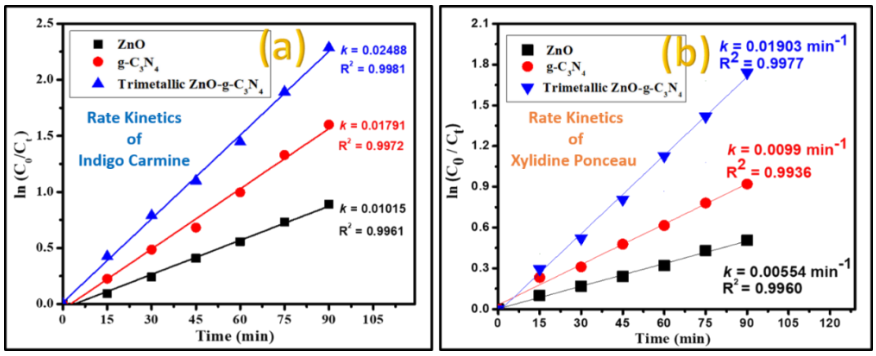

Figure 9. First-order kinetic plots for the degradation of (a) Indigo Carmine and (b) Xylidine Ponceau dyes using Bi_2O_3, Co_3O_4, and Fe_2O_3 co-doped ZnO-g-C_3N_4 under solar irradiation (reaction conditions: catalysts, 0.4 g/100 ml; dye concentration, 10 mg/L; pH, 8

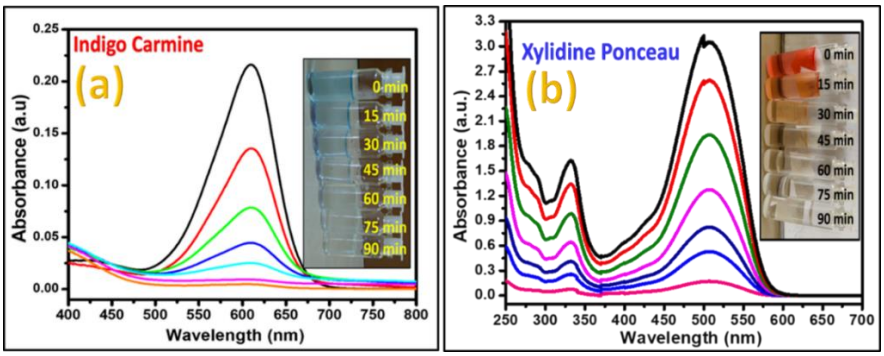

Figure 10. Visual monitoring of the progressive color fading of (a) Indigo Carmine and (b) Xylidine Ponceau solutions under sunlight in the presence of Bi_2O_3, Co_3O_4, and Fe_2O_3 co-doped ZnO-g-C_3N_4 (reaction conditions: catalysts, 0.4 g/100 ml; dye concentration, 10 mg/L; pH, 8.0)

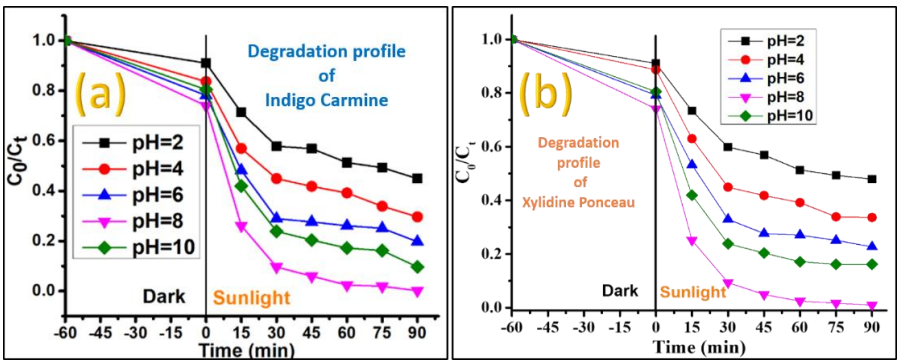

Figure 11. Effect of initial pH on the photocatalytic degradation efficiency of (a) Indigo Carmine and (b) Xylidine Ponceau using Bi_2O_3, Co_3O_4, and Fe_2O_3 co-doped ZnO-g-C_3N_4 under sunlight (reaction conditions: catalysts, 0.4 g/100 ml; dye concentration, 10 mg/L)

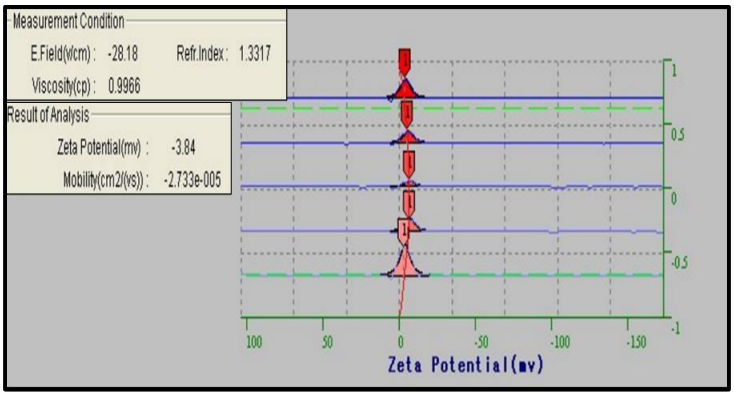

Figure 12. Zeta potential of Bi_2O_3, Co_3O_4, and Fe_2O_3 co-doped ZnO-g-C_3N_4 nanocomposite

3.8. Effect of catalyst dose

The influence of catalyst concentration on the photodegradation efficiency of Indigo Carmine (IC) and Xylidine Ponceau (XP) dyes using Bi_2O_3, Co_3O_4, and Fe_2O_3 doped ZnO-g-C_3N_4 under solar irradiation at pH 8 is depicted in Figures 13 (a) and (b). The optimal catalyst dose was determined to be 0.4 g/100 mL, at which the highest degradation efficiencies were achieved for both dyes. This concentration likely ensured an ideal dispersion of the photocatalyst, offering a maximum number of surface-active sites for dye adsorption and subsequent photocatalytic reactions, while maintaining sufficient light transmittance throughout the suspension [59]. At sub-optimal concentrations (0.1–0.3 g/100 mL), the reduced availability of photocatalyst limited the generation of electron–hole pairs and the associated reactive oxygen species (ROS), resulting in lower degradation efficiency. Conversely, at higher catalyst dosages (0.5–0.6 g/100 mL), a marginal decline in photocatalytic activity was observed. This phenomenon is attributed to the increased optical density of the suspension, which leads to significant light scattering and photon shielding effects, thereby reducing the penetration depth of incident light [60]. Additionally, higher catalyst loadings promote nanoparticle agglomeration, decreasing the effective surface area and hindering mass transfer between the dye molecules and the catalytic sites [61].

These observations underscore the importance of optimizing catalyst dosage to strike a balance between maximizing photocatalytic performance and minimizing adverse effects such as light attenuation and particle aggregation. Furthermore, such optimization ensures cost-effectiveness and sustainability for large-scale water purification applications.

3.9. Effect of dye concentration

The influence of initial dye concentration on the photocatalytic degradation of Indigo Carmine (IC) and Xylidine Ponceau (XP) anionic dyes was evaluated at a fixed pH of 8 and an optimized catalyst dosage of 0.4 g/100 mL under solar irradiation. As depicted in Figure 14, the degradation efficiency and overall photocatalytic performance exhibited a decreasing trend with increasing dye concentrations for both IC and XP.

This inverse relationship can be attributed to several interrelated factors. At higher dye concentrations (e.g., up to 25 ppm), the number of dye molecules in the solution significantly increases, leading to competitive adsorption on the limited active surface sites of the photocatalyst. This competition reduces the availability of those sites for the generation and interaction of reactive oxygen species (ROS), such as •OH and $O_2^{\bullet-}$, thereby diminishing the photocatalytic degradation rate [62].

Moreover, elevated dye concentrations result in increased solution opacity, which shortens the optical path length of incident photons and leads to excessive photon absorption by the dye molecules themselves rather than the catalyst surface.

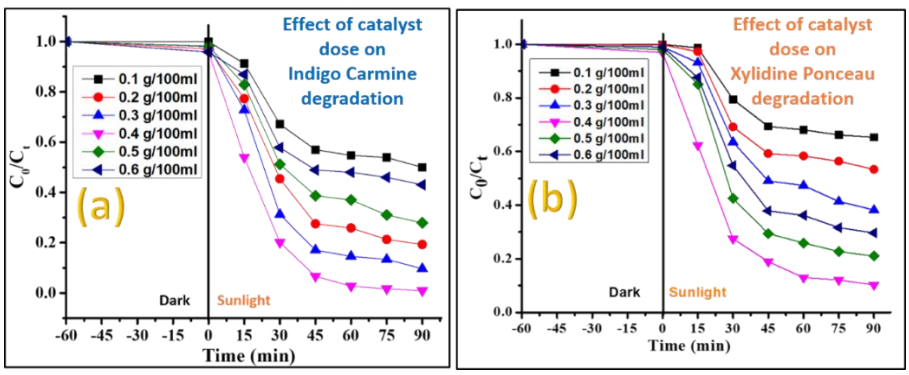

Figure 13. Influence of catalyst dosage on the photocatalytic degradation of (a) Indigo Carmine and (b) Xylidine Ponceau by Bi_2O_3, Co_3O_4, and Fe_2O_3 co-doped ZnO-g-C_3N_4 under solar light (reaction conditions: dye concentration, 10 mg/L; pH, 8.0)

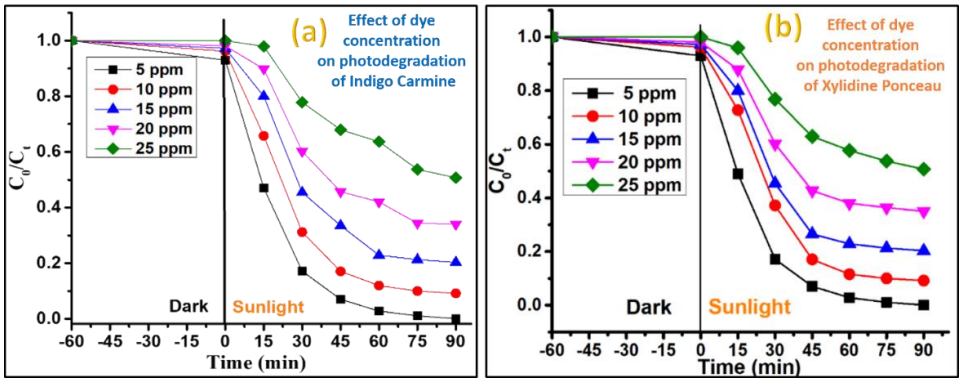

Figure 14. Effect of dye concentration on degradation efficiency of (a) Indigo Carmine and (b) Xylidine Ponceau using Bi_2O_3, Co_3O_4, and Fe_2O_3 co-doped ZnO-g-C_3N_4 under solar irradiation (reaction conditions: catalysts, 0.4 g/100 ml; pH, 8.0)

This light attenuation effect reduces the number of photons reaching the photocatalyst's surface, subsequently decreasing the photoexcitation of electron–hole pairs necessary for ROS formation. This phenomenon is particularly significant in heterogeneous photocatalysis driven by solar radiation, where the photonic flux is already diffuse and varies with time and weather conditions.

Conversely, at lower dye concentrations, the solution remains more transparent, allowing better light transmission and higher photon absorption by the photocatalyst. This enhances the rate of photo-generated charge carrier formation and subsequent dye degradation. Thus, the optimization of initial dye concentration is critical for maximizing photocatalytic efficiency and ensuring scalability in practical wastewater remediation systems [62,63].

To assess the extent of contaminant removal from water, TOC (Total Organic Carbon) analysis of both dyes was performed at regular intervals (0, 45, and 90 minutes) (Figure 15). This analysis not only confirmed the degradation of large organic molecules but also demonstrated the elimination of residual carbon skeletons, indicating a higher level of water purification. For Indigo Carmine (IC), the initial TOC value of approximately 4.12 mg/L decreased significantly to 0.0042 mg/L after 90 minutes. Similarly, Xylidine Ponceau (XP) showed a reduction in TOC from around 4.63 mg/L to 0.072 mg/L, validating the efficient removal of organic pollutants under alkaline conditions and with moderate catalyst loading.

3.10. Photocatalytic degradation mechanism

The generation of reactive oxygen species (ROS) is a fundamental aspect of semiconductor-based photocatalysis, governing the oxidative degradation of organic pollutants such as anionic dyes. In this study, the specific contributions of hydroxyl radicals (•OH), superoxide anions ($O_2^{\bullet-}$), and photogenerated holes (h^+) to the photodegradation of Indigo Carmine (IC) and Xylidine Ponceau (XP) were investigated using radical scavenger experiments. Photodegradation reactions were conducted under optimized conditions pH 8, 10 ppm dye concentration, and 0.4 g/100 mL catalyst loading under natural sunlight.

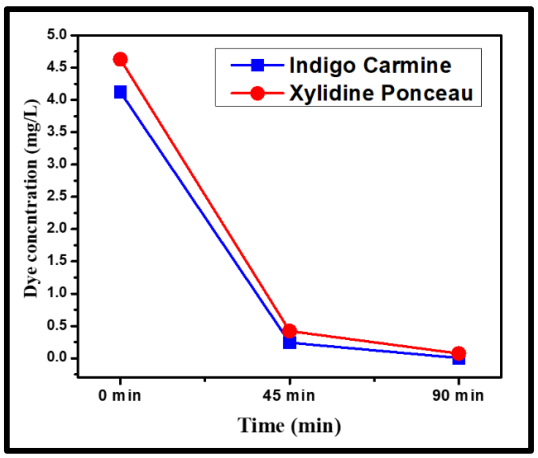

Figure 15. TOC analysis of dye samples ate regular intervals (reaction conditions: catalysts, 0.4 g/100 ml; pH, 8.0)

Scavengers were selectively introduced at a concentration of 500 mM: isopropyl alcohol (IPA) for •OH radicals, p-benzoquinone (BQ) for $O_2^{\bullet-}$, and ethylenediaminetetraacetic acid disodium salt (EDTA-2Na) for photogenerated holes (h^+).

As depicted in Figure 16, the addition of IPA led to a substantial reduction in degradation efficiency approximately 40% for both IC and XP indicating that •OH radicals are the primary reactive species responsible for the oxidative degradation of these dyes using the Bi_2O_3, Co_3O_4, and Fe_2O_3 co-doped ZnO–g-C_3N_4 photocatalyst. The suppression of color fading and degradation in the presence of IPA confirms the predominant role of hydroxyl radicals generated via surface-bound water oxidation under visible light excitation [64–66].

In contrast, the addition of EDTA and BQ resulted in comparatively marginal reductions in photocatalytic efficiency less than 10% suggesting limited roles for h^+ and $O_2^{\bullet-}$, respectively. The minimal impact of EDTA implies that the recombination of photogenerated holes is likely minimized through effective heterojunction formation within the trimetallic ZnO–g-C_3N_4 framework, while the lesser involvement of $O_2^{\bullet-}$ may

stem from suboptimal electron transfer to molecular oxygen in the conduction band [65,67].

These findings align with previously reported kinetic profiles in similar Z-scheme systems, where •OH radicals were identified as the dominant oxidizing species in dye degradation under solar irradiation. Based on this evidence, the relative contributions of ROS to the overall photocatalytic process are inferred as; •OH >> h^+ > O_2•$^-$. Upon solar excitation, efficient interfacial charge separation occurs within the ZnO–g-C_3N_4 heterojunction. The photogenerated electrons from g-C_3N_4 are transferred to ZnO's conduction band, while holes remain in the valence band of g-C_3N_4. Water molecules and surface hydroxyl groups are oxidized by h^+ to yield •OH radicals, which subsequently oxidize the dye molecules. Meanwhile, a minor fraction of electrons reduces O_2 to O_2•$^-$, which also contributes to degradation but with lower reactivity.

The remarkable similarity in the degradation of both the anionic azo dyes lies in their charges due to the extended conjugated aromatic systems and contain functional groups such as sulfonic acid groups and azo linkages. These common features likely result in similar adsorption behaviors on the catalyst surface and facilitate comparable reactive oxygen species (ROS) interactions during the photocatalytic process. Moreover, their structural resemblance allows both dyes to undergo similar degradation pathways under visible light irradiation, explaining the close range of degradation percentages and rate constants observed in this study.

The co-dopants (Bi_2O_3, Co_3O_4, Fe_2O_3) contribute by enhancing visible light absorption, introducing mid-gap states, and promoting effective charge separation. The ZnO–g-C_3N_4 heterojunction facilitates efficient interfacial charge transfer, where electrons from g-C_3N_4 migrate to ZnO, while holes remain in g-C_3N_4. These holes oxidize water to produce •OH radicals, which drive the degradation of the dyes. The similar degradation behavior of Indigo Carmine (IC) and Xylidine Ponceau (XP) is attributed to their structural resemblance, leading to comparable adsorption and ROS interactions.

3.11. Reusability study

The Bi_2O_3, Co_3O_4, and Fe_2O_3 co-doped ZnO/g-C_3N_4 nanocomposite demonstrates excellent reusability for the photocatalytic degradation of indigo carmine (IC) and xanthene-based (XP) anionic dyes under simulated sunlight at pH 8, with a catalyst loading of 0.4 g·100 mL^{-1} and dye concentrations of 10 ppm. As illustrated in Figure 17, the catalyst was recovered after each cycle via filtration and thermally regenerated at 150 °C for 2 hours to remove any residual organic matter. After four successive cycles, the catalyst maintained 78–80% degradation efficiency for both dyes, highlighting its structural stability and the effective synergy between doped ZnO and g-C_3N_4. This sustained photocatalytic activity is attributed to enhanced charge-carrier separation, which reduces electron–hole recombination, as well as the preservation of active surface sites due to the trimetallic doping. Minor efficiency losses observed after multiple cycles are likely caused by surface fouling from intermediate products and slight catalyst loss during the recovery process. These findings underscore the practical viability of the Bi_2O_3, Co_3O_4, and Fe_2O_3ZnO/g-C_3N_4 composites for long-term wastewater treatment applications.

3.12. Comparison of photocatalyst with other works

The comparison of the synthesized Bi_2O_3, Co_3O_4, and Fe_2O_3 doped ZnO-g-C_3N_4 catalyst with the extensive body of work on ZnO-graphitic carbon nitride (g-C_3N_4) composites proves to be challenging due to the uniqueness of this study. The distinctiveness of this work lies in its green ultrasonic synthesis method and the use of eco-friendly solar radiation for the photocatalytic degradation process. These features differentiate the current study from other reported approaches, highlighting both the sustainability and efficiency of the photocatalytic system. A comparative analysis of the degradation efficiency of Indigo Carmine (IC) and Xanthene-based Ponceau (XP) dyes by the synthesized catalyst is summarized in Table 4, offering a clear performance comparison to other systems in literature.

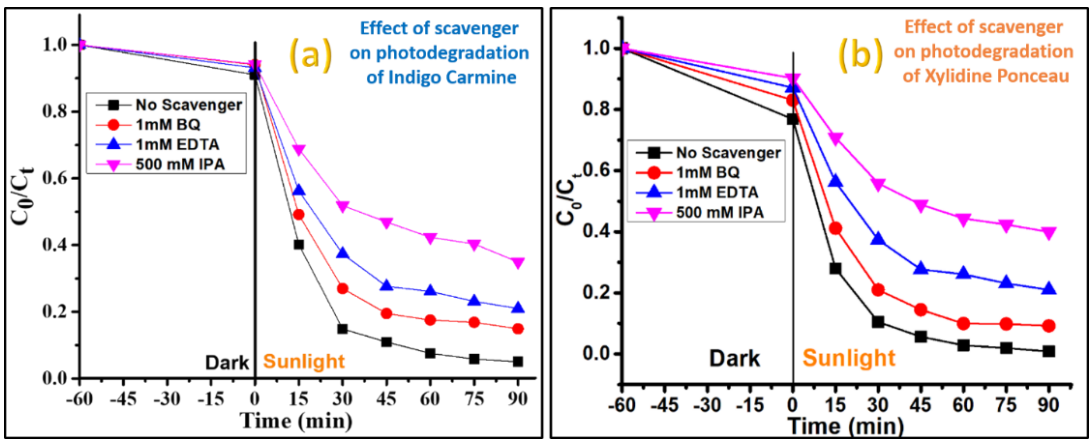

Figure 16. Effect of different scavengers on the photocatalytic degradation efficiency of (a) Indigo Carmine and (b) Xylidine Ponceau by Bi_2O_3, Co_3O_4, and Fe_2O_3 co-doped ZnO-g-C_3N_4 (reaction conditions: catalysts, 0.4 g/100 ml; dye concentration, 10 mg/L; pH, 8.0)

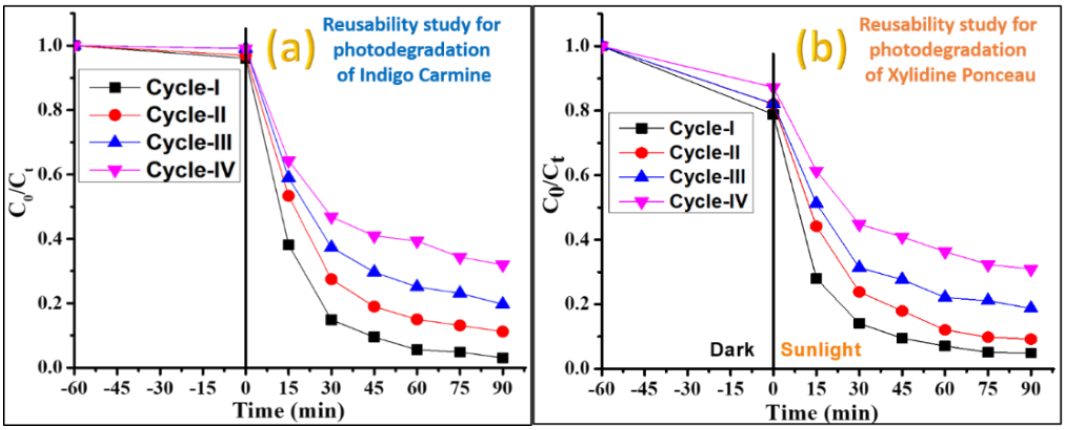

Figure 17. Reusability study of Bi_2O_3, Co_3O_4, and Fe_2O_3 co-doped ZnO-g-C_3N_4 nanocomposite for the degradation of (a) Indigo Carmine and (b) Xylidine Ponceau under sunlight (reaction conditions: catalysts, 0.4 g/100 ml; dye concentration, 10 mg/L; pH, 8.0)

Table 4. Comparative analysis of photocatalysts reported for the degradation of Indigo Carmine and Xylidine Ponceau dyes.

Sr. No.	Photocatalyst	Dye	Light Source	Time for Degradation	%Removal	Ref.
1.	ZnO-Bi_2O_3-g-C_3N_4 /H_2O_2	Indigo Carmine	Visible light	180 min	93%	[70]
2.	WO_3/CeO_2	Indigo Carmine	Visible light	120 min	30%	[71]
3.	Ag/ZnO	Indigo Carmine	Hg Lamp	120 min	96%	[72]
4.	ZnO	Xylidine Ponceau	UV	180 min	97%	[73]
5.	Fe^{2+}, Ag^{2+} + E. coli	Xylidine Ponceau	UVC (254 nm)	180 min	92%	[74]
6.	NiO	Xylidine Ponceau	Visible light	100 min	95%	[75]
7.	Bi_2O_3, Co_3O_4, and Fe_2O_3 doped ZnO-g-C_3N_4.	Indigo Carmine	Sunlight	90 min	98%	This Work
8.	Bi_2O_3, Co_3O_4, and Fe_2O_3 doped ZnO-g-C_3N_4.	Xylidine Ponceau	Sunlight	90 min	95%	This Work

4. Conclusions

This study successfully demonstrated an effective ultrasound-assisted green synthesis method for bismuth, iron, and cobalt-doped ZnO-g-C_3N_4 nanocomposites with doping. Structural and surface analyses using XRD, FT-IR, SEM/EDS, UV-DRS, and BET confirmed the successful incorporation of dopants and the formation of a nanocomposite with excellent optical and surface properties, which are critical for high catalytic activity. The nanocomposite exhibited outstanding photocatalytic performance, degrading Indigo Carmine (IC) and Xylidine Ponceau (XP) anionic dyes within 90 minutes under eco-friendly solar irradiation. The observed degradation efficiencies of 98.14% for IC and 94.82% for XP, along with rate constants of 2.488×10^{-2} min^{-1} and 1.903×10^{-2} min^{-1} respectively, followed first-order kinetics, indicating rapid photodegradation. Parametric studies on pH, catalyst dosage, and dye concentration helped optimize the degradation conditions. Scavenger tests confirmed hydroxyl radicals as the dominant reactive species, and reusability tests demonstrated the catalyst's stability over four cycles, affirming its cost-effectiveness and sustainability.

To further enhance the practical relevance of this work, future studies should investigate the catalyst's performance in real wastewater systems and explore its effectiveness against a broader spectrum of organic pollutants, including pharmaceuticals and industrial effluents. Implementation in pilot-scale treatment systems using natural sunlight can be considered to evaluate its scalability and environmental impact.

Funding

This research did not receive any specific grant from any funding.

Acknowledgments

The research leading to these results has received support from CIF, SPPU, Pune University for FTIR, SEM, EDS, XRD, ZPC, and BET characterization. IIT Bombay for Tem analysis. MERI Nashik for TOC analysis. Authors are also thankful to the Principal, K. V. N. Naik A, C and S College, Nashik and Principal Karmaveer Shantarambapu Kondaji Wavare Arts, Science and Commerece College for providing necessary laboratory facilities.

Authors Contribution
All authors have contributed equally to prepare the paper.

Availability of data and materials
The data that support the findings of this study are available from the corresponding author, upon reasonable request.

Conflict of interests
The authors declare that there is no conflict of interests regarding the publication of this paper.

References

[1] V. S. Raut, D. R. Malkhede, Y. R. Baste, S. G. Shinde, V. S. Shrivastava, *J. Alloys Compd. Commun.* (2025):100079. DOI: https://doi.org/10.1016/j.jacomc.2025.100079

[2] U. Shanker, M. Rani, V. Jassal, *Environ. Chem. Lett.* 15 (2017):623-42. DOI: https://doi.org/10.1007/s10311-017-0650-2

[3] B. Divband, A. Jodaie, M. Khatmian, *Iran. J. Catal.* 9 (2019):1. DOI: https://oiccpress.com/ijc/article/view/4025

[4] A. Yousefi, A. Nezamzadeh-Ejhieh, *Iran. J. Catal.* 11 (2021):3. DOI: https://oiccpress.com/ijc/article/view/3600

[5] S. Chu, M. Lin, D. Li, R. Lin, S. Xiao, *Ocean Eng.* 318 (2025):120139. DOI: https://doi.org/10.1016/j.oceaneng.2024.120139

[6] Y. Wang, S. Xia, K. Chen, J. Zhang, H. Tan, C. Yu, J. Cui, *ACS Nano.* 18 (2024):34403-14. DOI: https://doi.org/10.1021/acsnano.4c14039

[7] H. Wu, J. Li, L. Tian, F. Zhao, J. Yin, Y. Shao, *Chem. Eng. J.* 495 (2024):153608. DOI: https://doi.org/10.1016/j.cej.2024.153608

[8] Y. Yang, L. Zhang, C. Xiao, Z. Huang, F. Zhao, J. Yin, *Nanophotonics.* 13 (2024):443-55. DOI: https://doi.org/10.1515/nanoph-2023-0772

[9] B. Zhuang, Y. Yang, K. Huang, J. Yin, *Opt. Lett.* 49 (2024):6489-92. DOI: https://doi.org/10.1364/OL.540944

[10] Y. Yao, Y. Luo, Y. Yang, H. Sheng, X. Li, T. Li, Y. Song, *Energy.* 74 (2014):309-13. DOI: https://doi.org/10.1016/j.energy.2014.06.014

[11] S. Devaisy, J. Kandasamy, T. V. Nguyen, M. A. H. Johir, H. Ratnaweera, S. Vigneswaran, *Water.* 14 (2022):3708. DOI: https://doi.org/10.3390/w14223708

[12] A. Galdámez-Martinez, G. Santana, F. Güell, P. R. Martínez-Alanis, A. Dutt, *Nanomaterials.* 10 (2020):857. DOI: https://doi.org/10.3390/nano10050857

[13] J. Jiang, J. Pi, J. Cai, *Bioinorg. Chem. Appl.* 2018 (2018):1062562. DOI: https://doi.org/10.1155/2018/1062562

[14] P. Omprakash, P. Viswesh, *J. Solid State Sci. Technol.* 10 (2021):031009. DOI: https://doi.org/10.1149/2162-8777/abefaf

[15] N. Raeisi-Kheirabadi, A. Nezamzadeh-Ejhieh, *Int. J. Hydrogen Energy.* 45 (2020):33381-95. DOI: https://doi.org/10.1016/j.ijhydene.2020.09.028

[16] R. Fortulan, N. R. Kheirabadi, N. Raeisi-Kheirabadi, A. Nezamzadeh-Ejhieh, A. Chiolerio, A. Adamatzky, *Phys. Rev. E.* 110 (2024):034607. DOI: https://doi.org/10.1103/PhysRevE.110.034607

[17] P. B. Koli, M. D. Birari, S. A. Ahire, S. G. Shinde, R. S. Ingale, I. J. Patil, *Inorg. Chem. Commun.* 146 (2022):110083. DOI: https://doi.org/10.1016/j.inoche.2022.110083

[18] M. Sohail, U. Anwar, T. A. Taha, H. I. A. Qazi, A. G. Al-Sehemi, S. Ullah, H. Algarni, *Arab. J. Chem.* 15 (2022):104070. DOI: https://doi.org/10.1016/j.arabjc.2022.104070

[19] V. D. Pardeshi, V. J. Naukudkar, V. S. Raut, Y. R. Baste, K. D. Randhir, U. B. Kadam, R. S. Ingale, S. G. Shinde, *Second International Conference on Current Trends in Physics and Photonics (ICCTPP 2024).* SPIE; 2024:166–79. DOI: https://doi.org/10.1117/12.3045455

[20] L. Jiang, X. Yuan, Y. Pan, J. Liang, G. Zeng, Z. Wu, H. Wang, *Appl. Catal. B Environ.* 217 (2017):388-406. DOI: https://doi.org/10.1016/j.apcatb.2017.06.003

[21] M. Sayed, A. Khan, S. Rauf, N. S. Shah, F. Rehman, A. A. Al-Kahtani, J. A. Khan, *ACS Omega.* **5** (2020):30610-24. DOI: https://doi.org/10.1021/acsomega.0c04574

[22] S. Sagadevan, K. Pal, Z. Z. Chowdhury, M. E. Hoque, *J. Sol-Gel Sci. Technol.* 83 (2017):394-404. DOI: https://doi.org/10.1007/s10971-017-4418-8

[23] H. B. Dias, M. I. B. Bernardi, V. S. Marangoni, A. A. Bernardi, A. N. S. Rastelli, A. C. Hernandes, *Mater. Sci. Eng. C.* 96 (2019):391-401. DOI: https://doi.org/10.1016/j.msec.2018.10.063

[24] P. B. Koli, K. H. Kapadnis, U. G. Deshpande, U. J. Tupe, S. G. Shinde, R. S. Ingale, *Environ. Chall.* 3 (2021):100043. DOI: https://doi.org/10.1016/j.envc.2021.100043

[25] A. Norouzi, A. Nezamzadeh-Ejhieh, R. Fazaeli, *Mater. Sci. Semicond. Process.* 122 (2021):105495. DOI: https://doi.org/10.1016/j.mssp.2020.105495

[26] S. G. Shinde, M. P. Patil, G. D. Kim, V. S. Shrivastava, *J. Inorg. Organomet. Polym. Mater.* 30 (2020):1141-52. DOI: https://doi.org/10.1007/s10904-019-01273-2

[27] M. Ghaedi, A. Ansari, M. H. Habibi, A. R. Asghari, *J. Ind. Eng. Chem.* 20 (2014):17-28. DOI: https://doi.org/10.1016/j.jiec.2013.04.031

[28] A. Yousefi, A. Nezamzadeh-Ejhieh, *Iran. J. Catal.* 11 (2021):3. DOI: https://oiccpress.com/ijc/article/view/3600

[29] R. Prabhakar, S. R. Samadder, *J. Clean. Prod.* 168 (2017):1201-10.

DOI: https://doi.org/10.1016/j.jclepro.2017.09.063

[30] H. Wang, X. Liu, P. Niu, S. Wang, J. Shi, L. Li, *Matter*. 2 (2020):1377-413.
DOI: https://doi.org/10.1016/j.matt.2020.04.002

[31] R. S. Ingale, S. G. Shinde, K. A. Khamkar, P. B. Koli, S. A. Kulkarni, I. J. Patil, *Sensing Imaging*. 25 (2024):36.
DOI: https://doi.org/10.1007/s11220-024-00488-z

[32] S. D. Khairnar, A. N. Kulkarni, S. G. Shinde, S. D. Marathe, Y. V. Marathe, S. D. Dhole, V. S. Shrivastava, *J. Photochem. Photobiol*. 6 (2021):100030.
DOI: https://doi.org/10.1016/j.jpap.2021.100030

[33] K. C. Nwambaekwe, V. P. Batir, L. Dermenji, N. D. Curmei, E. Arushanov, E. I. Iwuoha, *Mater. Chem. Phys*. 301 (2023):127594.
DOI: https://doi.org/10.1016/j.matchemphys.2023.127594

[34] C. K. Nerkar, S. G. Shinde, V. S. Raut, S. A. Shaikh, S. S. Chobe, *J. Indian Chem. Soc*. 2025:101751.
DOI: https://doi.org/10.1016/j.jics.2025.101751

[35] A. P. Naik, H. Mittal, V. S. Wadi, L. Sane, A. Raj, S. M. Alhassan, A. Al Alili, S. V. Bhosale, P. P. Morajkar, *J. Environ. Manage*. 258 (2020):110029.
DOI: https://doi.org/10.1016/j.jenvman.2019.110029

[36] N. G. Shinde, R. D. Sandhanshiv, S. G. Shinde, *Mater. Today Proc*. 2023.
DOI: https://doi.org/10.1016/j.matpr.2023.05.173

[37] S. Naghdi, M. M. Shahrestani, M. Zendehbad, H. Djahaniani, H. Kazemian, D. Eder, *J. Hazard. Mater*. 442 (2023):130127.
DOI: https://doi.org/10.1016/j.jhazmat.2022.130127

[38] R. da Silva Fernandes, M. R. de Moura, G. M. Glenn, F. A. Aouada, *J. Mol. Liq*. 265 (2018):327-36.
DOI: https://doi.org/10.1016/j.molliq.2018.06.005

[39] P. B. Koli, S. G. Shinde, K. H. Kapadnis, A. P. Patil, M. P. Shinde, S. D. Khairnar, D. B. Sonawane, R. S. Ingale, *J. Indian Chem. Soc*. 98 (2021):100225.
DOI: https://doi.org/10.1016/j.jics.2021.100225

[40] S. Ghattavi, A. Nezamzadeh-Ejhieh, *Int. J. Hydrogen Energy*. 45 (2020):24636-56.
DOI: https://doi.org/10.1016/j.ijhydene.2020.06.207

[41] H. Derikvandi, A. Nezamzadeh-Ejhieh, *J. Mol. Catal. A Chem*. 426 (2017):158-69.
DOI: https://doi.org/10.1016/j.molcata.2016.11.011

[42] V. Pardeshi, V. Naukudkar, V. Raut, Y. Baste, K. Randhir, U. Kadam, R. Ingale, S. Shinde, *Second International Conference on Current Trends in Physics and Photonics (ICCTPP 2024)*. SPIE; 2024:166-79.
DOI: https://doi.org/10.1117/12.3045455

[43] S. Sharafzadeh, J. Zolgharnein, A. Nezamzadeh–Ejhieh, S. D. Farahani, *Surf. and Interfaces*. 2025:105917.
DOI: https://doi.org/10.1016/j.surfin.2025.105917

[44] A. Yousefi, A. Nezamzadeh-Ejhieh, *Iran. J. Catal*. 11 (2021):3.
DOI: https://oiccpress.com/ijc/article/view/3600

[45] M. Haghshenas, M. Mazloum-Ardakani, F. Tamaddon, A. Nasiri, *Int. J. Hydrogen Energy*. 46 (2021):3984-95.
DOI: https://doi.org/10.1016/j.ijhydene.2020.10.253

[46] N. Golestani, A. Nasiri, M. Hashemi, *Desalin. Water Treat*. 280 (2022):312-29.
DOI: https://doi.org/10.5004/dwt.2022.29118

[47] M. Pourshaban-Mazandarani, M. Ahmadian, A. Nasiri, A. Poormohammadi, *Appl. Water Sci*. 13 (2023):179.
DOI: https://doi.org/10.1007/s13201-023-02002-4

[48] A. Nasiri, M. Malakootian, N. Javid, *Desalin. Water Treat*. 248 (2022):134-48.
DOI: https://doi.org/10.5004/dwt.2022.28046

[49] M. A. Gharaghani, M. Samaei, H. Mahdizadeh, A. Nasiri, M. Keshtkar, A. Mohammadpour, A. M. Khaneghah, *Environ. Res*. 246 (2024):118128.
DOI: https://doi.org/10.1016/j.envres.2024.118128

[50] B. Manikandan, K. R. Murali, R. John, *Iran. J. Catal*. 11 (2021):1.
DOI: https://oiccpress.com/ijc/article/view/3578

[51] S. Sharafzadeh, J. Zolgharnein, A. Nezamzadeh–Ejhieh, S. D. Farahani, *Int. J. Hydrogen Energy*. 106 (2025):1429-42.
DOI: https://doi.org/10.1016/j.ijhydene.2025.02.031

[52] A. Zare, M. Oraki, *Iran. J. Catal*. 13 (2023):2.
DOI: https://doi.org/10.30495/ijc.2023.1983633.2003

[53] A. A. Alharbi, O. Aldaghri, B. A. El-Badry, K. H. Ibnaouf, F. Alfadhl, A. Albadri, *Opt. Mater*. 152 (2024):115443.
DOI: https://doi.org/10.1016/j.optmat.2024.115443

[54] S. G. Shinde, V. S. Shrivastava, *SN Appl. Sci*. 2 (2020):1-11.
DOI: https://doi.org/10.1007/s42452-020-2295-1

[55] N. A. Jamalluddin, A. Z. Abdullah, *Ultrason. Sonochem*. 18 (2011):669-78.
DOI: https://doi.org/10.1016/j.ultsonch.2010.09.004

[56] S. Rajabi, Z. Derakhshan, S. Maleky, A. Nasiri, B. Ahmadi, M. Feilizadeh, A. Mohammadpour, M. R. Samaei, M. Hashemi, *Int. J. Biol. Macromol*. 286 (2025):138375.
DOI: https://doi.org/10.1016/j.ijbiomac.2024.138375

[57] K. Azarshab, M. Hashemi, A. Nasiri, A. Khodabakhshi, *Appl. Water Sci*. 14 (2024):197.
DOI: https://doi.org/10.1007/s13201-024-02261-9

[58] S. Sharafzadeh, A. Nezamzadeh-Ejhieh, *Electrochim. Acta*. 184 (2015):371-80.
DOI: https://doi.org/10.1016/j.electacta.2015.09.164

[59] A. Sobhani-Nasab, M. Eghbali-Arani, S. M. Hosseinpour-Mashkani, F. Ahmadi, M. Rahimi-Nasrabadi, *Iran. J. Catal*. 10 (2020):2.
DOI: https://oiccpress.com/ijc/article/view/3548

[60] Z. Sabok-khiz, A. Nasiri, H. Daraei, *Environ. Technol. Innov*. 36 (2024):103759.
DOI: https://doi.org/10.1016/j.eti.2024.103759

[61] S. Rajabi, Z. Derakhshan, A. Nasiri, M. Feilizadeh, A. Mohammadpour, M. Salmani, S. H. Kochaki, H. Shouhanian, H. Hashemi, *Environ. Technol. Innov*. 35 (2024):103724.
DOI: https://doi.org/10.1016/j.eti.2024.103724

[62] A. Pourtaheri, A. Nezamzadeh-Ejhieh, *Chem. Eng. Res. Des*. 104 (2015):835-43.
DOI: https://doi.org/10.1016/j.cherd.2015.10.031

[63] N. Arabpour, A. Nezamzadeh-Ejhieh, *Process Saf. Environ. Prot*. 102 (2016):431-40.
DOI: https://doi.org/10.1016/j.psep.2016.04.025

[64] M. H. A. Fard, A. Nasiri, H. Daraei, *Appl. Water Sci*. 13 (2023):11.
DOI: https://doi.org/10.1007/s13201-023-02026-w

[65] S. Senobari, A. Nezamzadeh-Ejhieh, *J. Photochem. Photobiol. A Chem*. 394 (2020):112455.
DOI: https://doi.org/10.1016/j.jphotochem.2020.112455

[66] A. Yousefi, A. Nezamzadeh-Ejhieh, *Iran. J. Catal*. 11 (2021):3.

DOI: https://oiccpress.com/ijc/article/view/3600

[67] H. Derikvandi, M. Vosough, A. Nezamzadeh-Ejhieh, *Environ. Sci. Pollut. Res.* 27 (2020):27582-97.
DOI: https://doi.org/10.1007/s11356-020-08817-x

[68] S. G. Shinde, M. P. Patil, G. D. Kim, V. S. Shrivastava, *J. Environ. Chem. Eng*. 8 (2020):103769.
DOI: https://doi.org/10.1016/j.jece.2020.103769

[69] R. S. Ingale, S. G. Shinde, K. A. Khamkar, P. B. Koli, S. A. Kulkarni, I. J. Patil, *Sensing Imaging.* 25 (2024):36.
DOI: https://doi.org/10.1007/s11220-024-00488-z

[70] B. T. Huy, D. S. Paeng, C. T. B. Thao, N. T. K. Phuong, Y. I. Lee, *Arab. J. Chem.* 13 (2020):3790-800.
DOI: https://doi.org/10.1016/j.arabjc.2019.01.003

[71] D. Channei, K. Chansaenpak, S. Phanichphant, P. Jannoey, W. Khanitchaidecha, A. Nakaruk, *ACS Omega*. 6 (2021):19771-7.
DOI: https://doi.org/10.1021/acsomega.1c02453

[72] R. Kumar, S. Y. Janbandhu, G. K. Sukhadeve, R. S. Gedam, *Environ. Sci. Pollut. Res.* 30 (2023):98619-31.
DOI: https://doi.org/10.1007/s11356-022-22745-y

[73] M. El-Kammah, E. Elkhatib, S. Gouveia, C. Cameselle, E. Aboukila, *Sustain. Chem. Pharm*. 29 (2022):100753.
DOI: https://doi.org/10.1016/j.scp.2022.100753

[74] M. Marbaniang, J. E. Kumar, T. Mulai, W. Kharmawphlang, R. N. Sharan, M. K. Sahoo, *Chem. Select.* 9 (2024):e202401474.
DOI: https://doi.org/10.1002/slct.202401474

[75] N. M. Hosny, I. Gomaa, A. Abd El-Moemen, Z. M. Anwar, *J. Mater. Sci. Mater. Electron.* 31 (2020):8413-22.
DOI: https://doi.org/10.1007/s10854-020-03376-w